MTLA 43 (2025) 102510

Contents lists available at ScienceDirect

Materialia

journal homepage: www.elsevier.com/locate/mtla

Full Length Article

Amorphous complexion-aided sintering enables scalable processing of bulk nanocrystalline Cu-Zr with high strength and compressive plasticity

Esther C. Hessong [a,1], Tianjiao Lei [a,b,1], Brandon Fields [a], Raphael Pierre Thiraux [a], Brad L. Boyce [c,d], Timothy J. Rupert [a,e,f,*]

[a] Department of Materials Science and Engineering, University of California, Irvine, CA 92697, USA
[b] Metallurgical and Materials Engineering, University of Alabama, Tuscaloosa, AL 35401, USA
[c] Center for Integrated Nanotechnologies, Albuquerque, NM 87185, USA
[d] Sandia National Laboratories, Albuquerque, NM 87185, USA
[e] Hopkins Extreme Materials Institute, Johns Hopkins University, Baltimore, MD 21218, USA
[f] Department of Materials Science and Engineering, Johns Hopkins University, Baltimore, MD 21218, USA

ARTICLE INFO

Keywords:
Bulk nanocrystalline alloy
Compression testing
Sintering
Strengthening

ABSTRACT

Nanocrystalline alloys can have exceptional strengths, yet due to limited microstructural stability it is difficult to fabricate bulk pieces through traditional processing routes that retain nanosized grains. In this study, centimeter-sized Cu-Zr alloy pellets were fabricated via a simple and improved powder metallurgy processing route. Different consolidation temperatures and times were employed to investigate the effect of amorphous grain boundary complexions on densification and the resulting mechanical properties. Bulk compression tests were carried out, with the samples that were hot pressed at 900 °C for 10 h exhibiting an excellent combination of average yield strength of 722 ± 45 MPa and average failure strain of 25.3 ± 2.4 %. Therefore, we find that a powder processing route which enables amorphous complexion-assisted sintering leads to samples that (1) reach full density without requiring quenching treatments or other complex processing, (2) demonstrate appreciable plasticity, and (3) have strength that competes with commercially available high-strength Cu alloys.

1. Introduction

Copper alloys are widely used in the automobile, electrical, and electronics industries for their high electrical conductivity and useful mechanical properties [1–3]. Commercially available Cu-Be alloys have some of the highest strengths (~1400 MPa) [4], yet Be presents serious human health hazards in production and high-strength alloys without this element are needed. Cu-rich alloys without Be that reach over 1000 MPa include nano-twinned Cu [5,6], Cu-Ti [7–9], and Cu-Ni-Zn-Al [10], although these materials have been limited to small sample sizes such as film thicknesses of < 25 μm, wires, or plates with millimeter thicknesses. These examples generally achieve strength through nanostructuring, yet economically viable processing for commercial bulk applications (e.g., power grid systems) can be challenging. Common methods for bulk manufacturing involve severe plastic deformation (e.g., equal channel angular extrusion [11,12], high pressure torsion [13,14], and surface mechanical attrition [15,16]). Those techniques introduce extensive deformation defects that can be unstable in subsequent thermal environments, and also those techniques can have difficulties in attaining grain sizes <<100 nm.

An alternative processing option that results in nanocrystalline alloys that can subsequently be shaped and scaled up is powder metallurgy. Powder metallurgy has many industrial applications due to potential for scalability and fabrication of high-quality parts at low costs, yet residual porosity after compaction or consolidation can limit structural applications. Porosity is one of the dominant issues that deteriorates mechanical properties and has prevented powder metallurgy from being adopted for critical components in aerospace and other applications [17], as it can reduce strength, fatigue resistance, and corrosion resistance in powder metallurgy materials due to the weak bonding strengths between unsintered particles. For example, an only 4.2 % reduction in density for ball milled, Y_2O_3-reinforced Cu was found to result in reduction of the yield strength by ~60 MPa in Ref [18]. These authors noted that post-milling thermal treatment at 923 K (~0.6 of the

* Corresponding author.
E-mail address: tim.rupert@jhu.edu (T.J. Rupert).
[1] These authors contributed equally to this work.

https://doi.org/10.1016/j.mtla.2025.102510
Received 21 May 2025; Accepted 31 July 2025
Available online 31 July 2025
2589-1529/© 2025 Acta Materialia Inc. Published by Elsevier Inc. All rights are reserved, including those for text and data mining, AI training, and similar technologies.

homologous temperature of Cu) for 15 h increased the density to 97 %. While elevated temperatures can reduce the porosity, high temperatures and long treatment times can also lead to grain coarsening [19] and subsequently reduced strengths [20–22].

Nanostructuring is a promising route for the production of high-strength Cu alloys as the large volume fraction of grain boundaries can act as obstacles to dislocation motion. However, the processing routes for producing nanograined metals in bulk quantities typically involve high temperatures and pressures, which again brings concerns associated with microstructural coarsening and strength reduction. For example, Cu-Ta alloy powders synthesized via mechanical alloying were consolidated at different temperatures, where the highest temperature of 900 °C led the Cu grains to coarsen by ~27 % and strength to be lowered by 40 % [23]. Similarly, Botcharova et al. observed coarsening of both the nanocrystalline Cu-rich grains and Nb-rich particles in a nanostructured Cu-Nb alloy. Annealing at 900 °C resulted in a decrease of 13 % in the ultimate compressive strength [24]. Thus, there is a need for the ability to consolidate nanocrystalline materials into bulk pieces while retaining high strengths to enable processing scalability for real-world applications.

Stabilization of nanocrystalline microstructures can be achieved by alloying, where the dopants kinetically impede grain boundary migration [25] and/or thermodynamically decrease grain boundary energy [26]. Introducing dopants species with a tendency to segregate to grain boundaries is especially advantageous for pinning boundaries, such as in nanocrystalline Cu-Ta where Ta clusters segregate and prevent grain growth [27]. Similarly, Sikdar et al. showed that uniformly distributed intermetallics in Cu-Zr can cause pinning and that Zr segregated to the grain boundaries inhibits grain growth [28]. In a similar Cu-Zr alloy, Donaldson and Rupert showed that Zr segregation can promote pre-melting transitions at grain boundaries to form amorphous complexions, which can stabilize the nanocrystalline structure at temperatures close to the melting point of the solvent [29]. In addition, amorphous, Zr-enriched complexions form between 750 °C and 850 °C in Cu-Zr powders [30]. Thus, by consolidating Cu-Zr bulk pieces above 850 °C, amorphous complexions should be present within the sample and aid in sintering the powder particles. While grain sizes can be stabilized and density improved, no studies to date have reported on the mechanical response of these alloys in bulk form.

Based on previous sintering studies of nanocrystalline Cu-Zr, two consolidation conditions were selected for this study to isolate the effect of improved sintering on the mechanical behavior of bulk nanocrystalline Cu-Zr alloys. The presence of amorphous complexions during consolidation at 900 °C led to full densification of the pellet with no observed porosity. The internal microstructure reveals only mild matrix grain coarsening from 40 nm to 101 nm even under a higher consolidation temperature and much longer pressing time. Full density and the fine final grain size gives rise to excellent mechanical properties with an average yield strength of 722 ± 45 MPa and average failure strains of 25.3 ± 2.4 %. In addition to amorphous complexion-enabled sintering to full density, the observed substantial plasticity can be partially attributed to limited crack propagation length and features similar to kink bands.

2. Experimental section

Nanocrystalline Cu-3 at. % Zr alloys were fabricated by ball milling powders of Cu (Alfa Aesar, 99.99 %, −170 + 400 mesh) and Zr (Micron Metals, 99.7 %, −50 mesh) for 10 h. Ball milling was conducted in a SPEX SamplePrep 8000 M high-energy ball mill in a glovebox filled with Ar gas at an O_2 level <0.05 ppm to minimize oxidation. A hardened steel vial and milling balls were used, with a ball-to-powder weight ratio of 10:1. In order to prevent excessive cold welding, 1 wt.% stearic acid was added as a process control agent. After milling, the alloyed powders were transferred into a 14 mm inner diameter graphite die set and consolidated into cylindrical bulk pellets using an MTI Corporation OTF-1200X-VHP3 hot press with a vertical vacuum-sealed quartz tube furnace and a hydraulic press. Cold pressing was first performed under 25 MPa and room temperature for 10 min, followed by hot pressing. Two sets of conditions were used for consolidation: (1) 800 °C and 50 MPa for 1 h and (2) 900 °C and 50 MPa for 10 h. A heating ramp of 10 °C min^{-1} was used until the maximum consolidation temperature was reached, and the pellets were naturally cooled down to room temperature inside the hot press, which typically took >4 h. The dimensions of all bulk samples were ~1 cm in height and 1.4 cm in diameter.

For quasi-static bulk compression testing, cylinders with 3 mm diameter and 6 mm height were sectioned via electrical discharge machining from the as-consolidated pellets. Compression tests were conducted at an initial rate of 1×10^{-3} s^{-1} on an Instron 5985 frame equipped with a 250 kN load cell and strain calculations were obtained from sample displacement. Six cylindrical specimens were tested for each condition to check for consistency and yield strengths were extracted using the common 0.2 % offset method. For porosity investigation, both optical microscopy and computed tomography scans were employed. Optical micrographs were taken of the cross section of each sample, which was first ground with SiC grinding paper down to 1200 grit and then auto-polished with monocrystalline diamond suspension down to 0.25 μm. To examine whether larger pores formed within samples, computed tomography (CT) scans were performed using an Xradia 410 Versa CT scanner (Zeiss, USA) with a voltage of 80 kV and power of 15 W, achieving a resolution of 13.6 μm. All CT scans were post-processed using ImageJ and no pores larger than 30 μm were observed for either of the consolidation conditions studied here.

Microstructural characterization was carried out using a variety of techniques. First, X-ray diffraction (XRD) measurements were conducted to obtain phase composition, phase fraction, and mean grain sizes. XRD was performed using a Rigaku Ultima III X-ray diffractometer, with a Cu Kα radiation source operated at 40 kV and 30 mA and a one-dimensional D/teX Ultra detector. The XRD scans were analyzed using an integrated powder X-ray analysis software package (Rigaku PDXL). Scanning electron microscopy (SEM) imaging for fracture surface examination and backscattered electron (BSE) imaging for intermetallic investigation were performed in an FEI Quanta 3D FEG dual-beam SEM/Focused Ion Beam (FIB) microscope. TEM lamella were lifted out using the FEI Quanta 3D FEG dual-beam SEM/FIB equipped with Ga^+ ion beam and OmniProbe. Bright-field (BF) and high-angle annular dark field (HAADF) scanning transmission electron microscopy (STEM) were used to study grain sizes and carbides inside of a JEOL JEM-2800 S/TEM operated at 200 kV and equipped with a Gatan OneView IS camera.

3. Results and discussion

3.1. Porosity and microstructural stability

Fig. 1(a) shows the Cu-Zr pellet after hot pressing at 800 °C for 1 h, where some visible pores appear on the side surface that was in contact with the pressing die. Fig. 1(b) shows the cylindrical specimens that were extracted for bulk compression tests. Optical images in Fig. 1(c) of the cross-sections show that the pores (darker areas) are located between particles (brighter areas), totaling ~20 % porosity and indicating that the 800 °C for 1 h processing condition is not sufficient to achieve full density for the Cu-Zr alloy. After being consolidated at 900 °C for 10 h, the Cu-Zr pellets were found to be 100 % dense with zero pores observed in Fig. 1(d). Although no pores were observed for this hot-pressing condition, the micrographs still exhibit two types of contrast, suggesting that either some difference in oxidation state exists or that different phases formed in the sample. For the present Cu-Zr system, the concentration of Zr is higher than the equilibrium solubility, meaning that different contrast could be due to intermetallic phases. In addition, carbide phases have been observed in Cu-rich alloys processed by ball milling and hot pressing [29,30], which could appear with a different contrast from the matrix. Optical microscopy cannot provide an answer

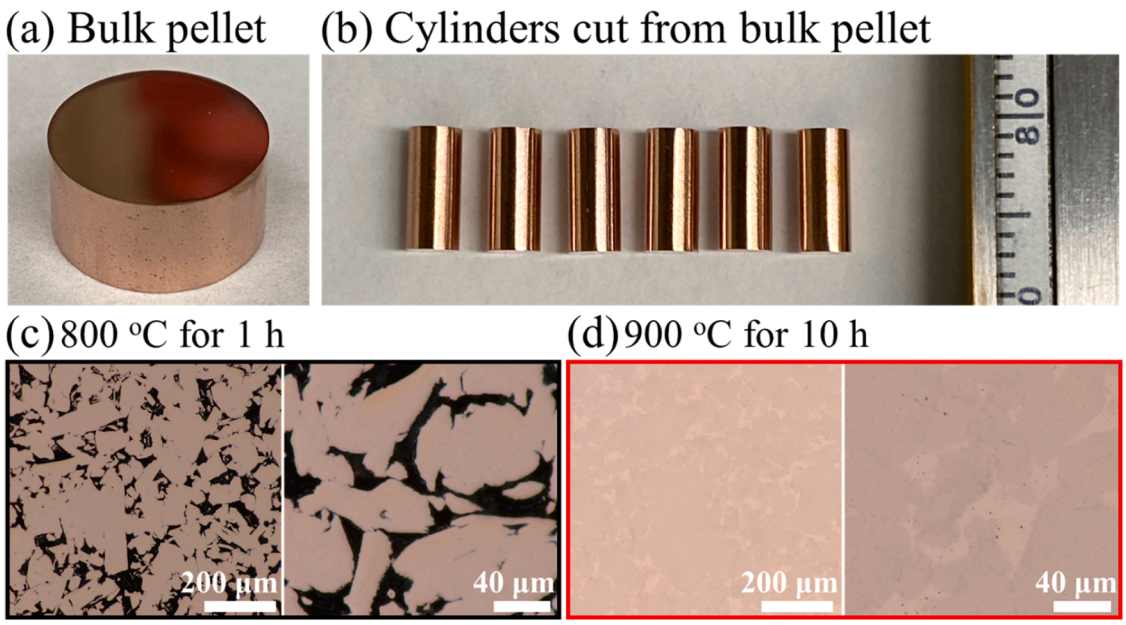

Fig. 1. (a) A Cu-Zr pellet after hot pressing under 800 °C for 1 h. (b) Cylindrical specimens for compression testing. All specimens are 3 mm in diameter and 6 mm in height, with an aspect ratio of 2. Cross-sectional optical micrographs correspond to hot-pressing conditions of (c) 800 °C for 1 h and (d) 900 °C for 10 h.

to this question, motivating subsequent XRD and TEM experiments.

Fig. 2(a) presents XRD scans of the Cu-Zr alloys for the two hot-pressing conditions, where face-centered cubic (FCC) Cu peaks are prominent as the majority phase. In addition to the Cu matrix, several small peaks exist. These peaks are identified as zirconium carbide (ZrC) based on the peak position and intensity. The carbide phase likely formed because of the stearic acid ($C_{18}H_{36}O_2$) added during the ball milling process as a process control agent. Fig. 2(b) shows a BF-STEM micrograph, which gives information on the morphology and size of the matrix grains. The grains possess a relatively equiaxed shape and the

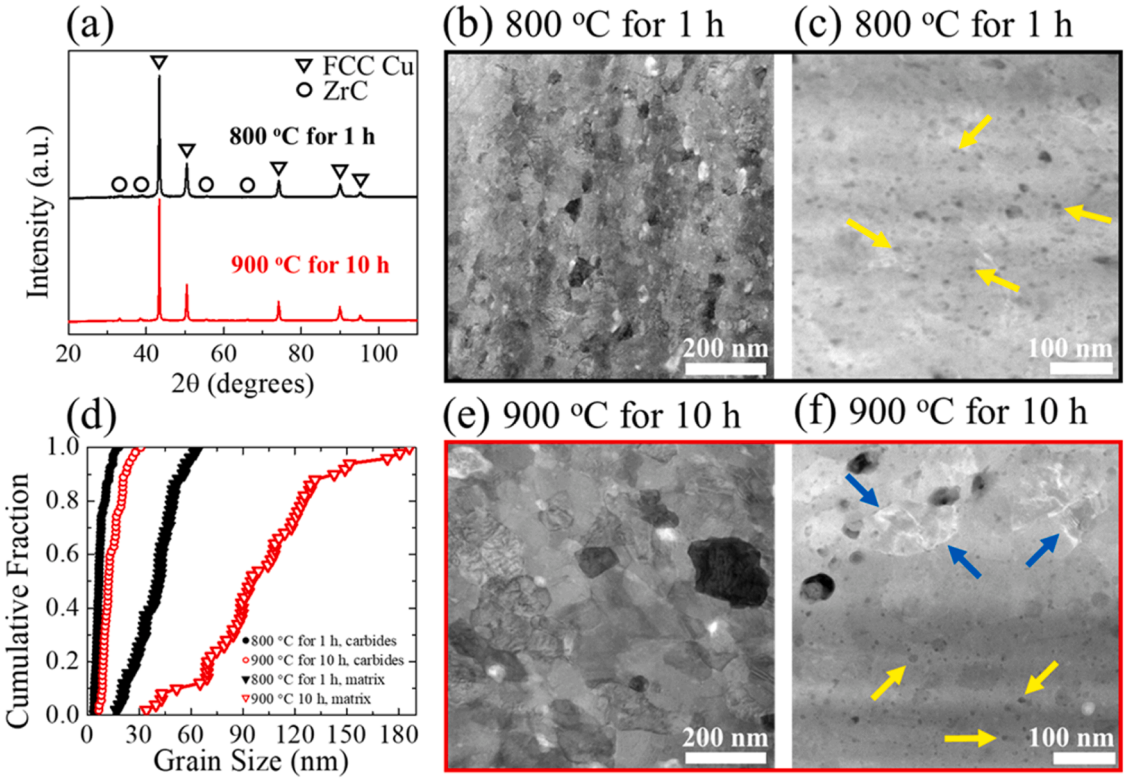

Fig. 2. Microstructural characterization for Cu-Zr alloys. (a) XRD scans showing that both hot-pressing conditions result in a primary FCC Cu phase, with some secondary impurity phases. (b) Low-mag BF-STEM and (c) high-mag HAADF-STEM micrographs showing matrix grains and carbide precipitates, respectively, for the 800 °C for 1 h sample. (d) Matrix and carbide grain size analyzed from STEM data for both hot-pressing conditions, with at least 50 measurements for each. (e) Low-mag BF-STEM and (f) high-mag HAADF-STEM images presenting matrix grains and precipitates for the 900 °C for 10 h sample, respectively. Yellow arrows indicate carbides and blue arrows indicate examples of Zr enrichment at the grain boundaries.

average matrix grain size is 40 ± 12 nm. The STEM measurement is close to the value obtained from XRD of 26 nm. Fig. 2(c) is a higher magnification HAADF-STEM image, where the secondary carbide phases are indicated by yellow arrows. These precipitates have a spherical shape with sizes ranging from 3–18 nm and an average diameter of 7.7 ± 3.3 nm, which is in close agreement with the XRD measurement of 5.4 nm. Most of these precipitates are at grain boundaries, while a select few also sit within the matrix grains. At least 50 measurements for both the matrix and carbide grain sizes were taken from STEM data for both hot-pressing conditions, with the results summarized in the cumulative distribution plot in Fig. 2(d).

A representative BF-STEM micrograph in Fig. 2(e) revealed that the matrix grains remained very fine (101 ± 34 nm), while the precipitates, indicated by yellow arrows on the HAADF-STEM micrograph in Fig. 2(f), coarsened to an average size of 14.4 ± 5.7 nm in diameter. The BF-STEM micrograph in Fig. 2(e) shows the matrix grains with nanocrystalline sizes and equiaxed shapes; the HAADF-STEM micrograph presented in Fig. 2(f) shows the precipitates more clearly. Revisiting the question of contrast in Fig. 1(d), there are no intermetallic phases observed and the carbides that were found are many orders of magnitude finer than the contrast changes observed. This suggests that the contrast variations shown in Fig. 1(d) represent the original powder particles and the regions filled by sintering. Other researchers have observed oxidation around unsintered particles that is removed after sintering processes [31,32], so it is possible oxidation is also the source of varying contrast here. The small grain size of the matrix FCC phase indicates an excellent thermal stability of the Cu-Zr system under prolonged treatment at a homologous temperature of 0.94. The thermally stable microstructure is primarily due to the grain boundary segregation of Zr and the formation of the amorphous grain boundary complexions during annealing [30], yet some additional pinning effect comes from the carbide precipitates at grain boundaries (Fig. 2(c, f)). Fig. 2(f) shows a HAADF image of the grain structure, where the brighter regions indicated by blue arrows signal Zr enrichment as contrast is proportional to atomic mass. Grain boundary segregation of Zr has been reported previously for Cu-Zr alloys (see, e.g., Ref [33]). Because amorphous complexions are thermodynamically stable at high temperatures, their formation is beneficial for microstructural stability by reducing the grain boundary energy during the annealing process. The amorphous complexions also improve the sintering during the consolidation step, as shown by Donaldson and Rupert [29]. It is important to note though that these amorphous complexions are not retained in the cooled pellet samples, as rapid quenching is needed to freeze them into the microstructure, but Zr segregates at both ordered grain boundaries and amorphous complexions [33]. The slow cooling in the hot press means that the grain boundaries revert back to an ordered state. For future optimization, it may be desirable to retain the amorphous complexions, or introduce an intermediate heat treatment to induce Zr segregation, which would also aid in limiting grain growth during sintering.

3.2. Compressive deformation behavior of bulk Cu-Zr pellets

Fig. 3 shows engineering stress-strain curves for both hot-pressing conditions, which exhibited dramatically different behavior. For the samples hot-pressed at 800 °C for 1 h, premature failure is found where the stress drops dramatically after yield and an average compressive strength of 459 ± 15 MPa is measured. Although the grain sizes were small for this processing condition, many pores remained in the sample (Fig. 1(c)). Hence, the low strength and plasticity are most likely due to the high porosity, which will be discussed below. For the 900 °C for 10 h sample, the yield strength was 722 ± 45 MPa with failure strain of 25.3 ± 2.4 % measured. The combination of high strength and appreciable plasticity is noteworthy. For example, a Cu-Zr metallic glass sample tested under compression exhibited a higher strength of ~2 GPa, but very little plastic strains, ranging from 0.1 % to a maximum of 7.5 % [34]. The average grain size for the 900 °C for 10 h condition (101 nm)

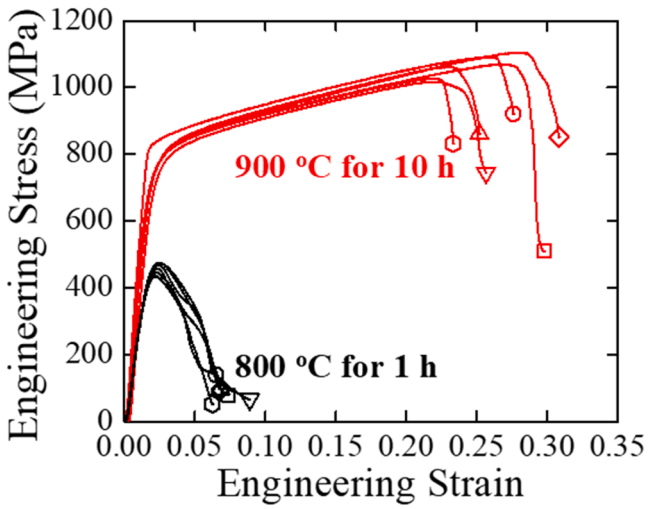

Fig. 3. Engineering stress-strain curves of bulk Cu-Zr samples for 800 °C for 1 h (black) and 900 °C for 10 h (red) hot pressing conditions.

suggests a strength of 403 MPa according to the Hall-Petch relation, meaning that grain size strengthening is the dominant mechanism [35]. Additional contributions include strengthening from Zr grain boundary segregation and from the carbide nanoprecipitates. We remind the reader that, while amorphous grain boundary complexions were present during sintering, the slow cooling process used here means they have transitioned back to ordered grain boundaries by the time they are investigated in this study. Vo et al. showed that grain boundary segregation that decreases grain boundary energy can have a pronounced effect on the yield strength of nanocrystalline metals [36]. In addition, carbide nanoprecipitates dispersed throughout Cu alloys can increase yield strength, ultimate tensile strength, and hardness [37]. The carbide strengthening contribution was estimated to be ~250 MPa using the equations from Ref [37], with the volume fraction of carbides equal to 4.1 % from this work. If an additive strengthening effect is assumed, then Zr segregation would be responsible for the remaining ~50–100 MPa of strength. Although the stress-strain curves exhibited apparent hardening in Fig. 3, this is a consequence of the compressive loading mode. A maximum stress of 693 MPa is calculated if the final sample cross-sectional area is used, which is close to the yield stress. Consequently, the increasing engineering stress after yielding is simply geometric due to the increasing cross-sectional area during compression and these materials do not exhibit noticeable strain hardening.

The strengths measured here for a Cu alloy are outstanding, as a simple process route is used and a relatively affordable alloying element is used. Most high strength Cu alloys require expensive processing routes and/or alloying elements. Fig. 4 compares the cost of Cu-based commercial alloys with their yield strengths. The strength of the Cu-Zr alloy in this study competes with three commercial alloys: Glidcop, Cu-TiB_2 metal matrix composite Mixalloy, and Cu-Be-based alloys. The highest reported yield strength for Glidcop from the manufacturer is 655 MPa for a plate that is 0.15 mm thick, and Glidcop AL-15 has a yield strength of 450 MPa [38], below the strength of our Cu-Zr alloys. Mixalloy is no longer manufactured due to a complex processing route of spin casting, compaction, and extrusion that was more expensive relative to other commercial operations [39]. Compared to Cu-Be-based alloys, this Cu-Zr alloy is significantly cheaper per kilogram. Zr is less susceptible to supply chain vulnerabilities than Be [40], which can result in price fluctuations that vary by an order of magnitude. Additionally, despite Be's high strength and low density, manufacturing Be materials has been shown to be carcinogenic and associated with severe respiratory diseases [41]. These other three Cu-based alloys therefore each have significant drawbacks, while all the other commercial alloys have significantly lower strengths than the Cu-Zr in this work.

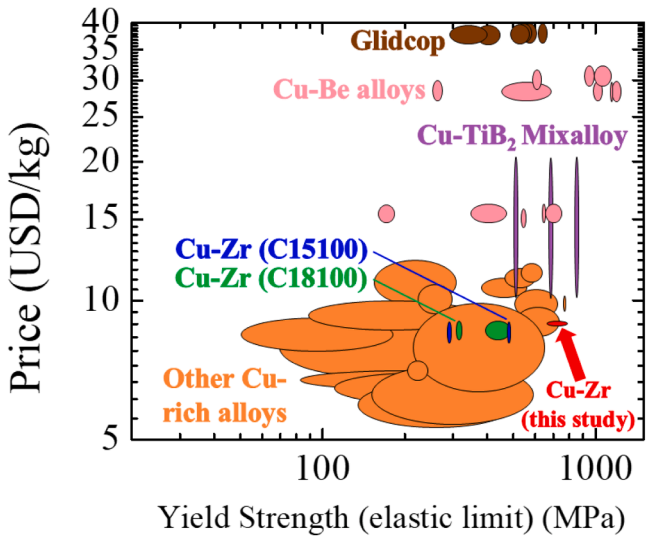

Fig. 4. Ashby-type plot showing price plotted against the yield strength for different commercial Cu-based alloys. The Cu-Be alloys (pink) have the highest strengths, followed by the discontinued Cu-TiB_2 Mixalloy (purple), and finally the Cu-Zr in this study (red).

Other research groups have fabricated bulk nanocrystalline Cu alloys that achieve strengths above 1000 MPa, yet the processing routes tend to be more complicated and limiting. Hornbuckle et al. prepared Cu-Ta-Li with yield strength ~1100 MPa via cryogenic milling and consolidated to bulk (3 mm diameter) using equal channel angular extrusion (ECAE) [38]. Similarly, Srinivasan et al. prepared nanocrystalline Cu-Ta with cryomilling and ECAE, reaching yield strengths under quasistatic loading up to ~1200 MPa [42]. However, ECAE requires specialized dies to control the angle through which the sample is sheared during deformation and often multiple extrusion passes are needed to create an equiaxed microstructure [43]. This processing pathway also limits the sample dimensions, as the specimen must be sheared through an angled opening and high levels of shear strain are typically sought, with extruded billets typically having cross sectional dimensions of millimeters and therefore still quite small for industrial production of structural material [44]. In contrast, hot pressing can create much larger sample dimensions. For example, Lister et al. [45] reported on a Ti-6Al-4V sample which was 3.2 cm in diameter with hot-pressing. Industrial hot-pressing equipment can be found for even larger samples up to 2 m. Industrial scale-up of ECAE has not occurred to this same extent. Another Cu alloy with nanoprecipitates reached a yield strength of 1086 MPa and was fabricated by melting in an induction furnace under N_2, cast, and hot rolled by 70 % reduction, which results in a plate ~1 cm thick [46]. Thus, we demonstrate here that the simple processing route of ball milling and consolidation at a temperature sufficient to activate amorphous grain boundary complexions can produce a centimeter-sized Cu-rich alloy with very high strength and low cost. For industrial applications, only a larger press would be needed to make larger samples. Further, complexion-aided sintering can be extended to other alloy systems with known amorphous complexion formation to produce high-quality bulk nanocrystalline materials without compromising strengths. Such alloys would be potentially useful for high-performance mechanical and electrical equipment in aerospace and magnet designs [47].

3.3. *Fractography and possible failure mechanisms*

Representative failed samples after compression testing are shown in Fig. 5. The 800 °C for 1 h samples crumbled, with individual particles exposed on the fractured surface in Fig. 5(a). Such behavior is attributed to the specimens having extensive porosity. Cracks were observed running along the compression axis with corresponding fracture planes running perpendicular to the compression axis – these "splitting" fractures correspond to maximum tensile strain and mode-I cracking under uniaxial compressive loading. The 900 °C for 10 h showed very different macroscopic shape change (barreling), microscopic deformation mode (kink-bands), failure plane (shear), and fractographic features. Those samples barreled out, with an example shown in Fig. 5(b). A dominant shear band is observed in this sample that goes from the top left to middle right, while several small shear bands are also observed. This ductile mode of failure is described as single-plane catastrophic shear in Ref [48]. Fig. 5(c) shows a magnified image of the side surface, revealing regions of ~30–40 μm in size with cracks propagating between them. These regions are orders of magnitude larger than the grain size, but similar to the original powder particle sizes and contrast variations shown in Fig. 1(d), suggesting that fracture occurs along the interfaces between the powder particles. Interestingly, each region contains many streaks with a common direction, where the streaks change directions between adjacent regions, giving rise to cracks with different orientations. It is worth noting that these features were observed on the entire sample surface, providing an additional reason for the excellent

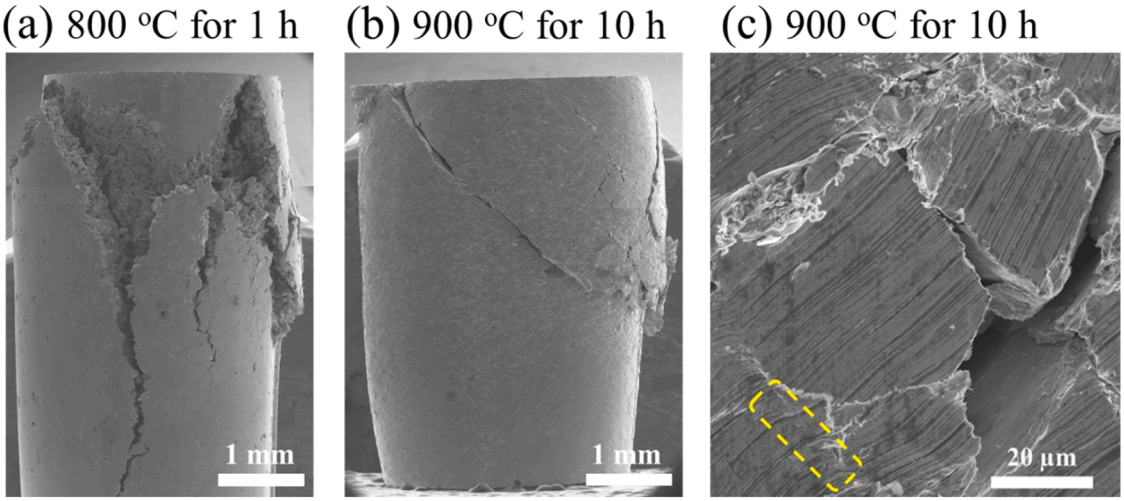

Fig. 5. SEM micrograph of representative deformed sample for (a) 800 °C for 1 h and (b) 900 °C for 10 h conditions. The former condition did not yield full density as individual particles can be observed on the fracture surface. The 900 °C for 10 h sample experiences a dominant shear band, where a magnified view (c) reveals kink band features (enclosed in dashed lines) on the sample surface.

plasticity because sample failure was drastically delayed due to the much smaller crack length than the sample dimension.

Features similar to kink bands were also observed in some regions, with examples enclosed in dashed lines in Fig. 5(c). Kink bands are often observed in materials with dramatically anisotropic crystal structure, such as hexagonal close packed systems, because of the strong dependence of mechanical properties on crystallographic direction [49,50]. Kinking does not usually occur in cubic metals due to the presence of multiple slip systems preventing the extensive single-slip needed for large rotations. However, as the grain size decreases to the nanoscale, the kinking mechanism has been occasionally observed in cubic systems. For example, Nizolek et al. observed that when the layer thickness was reduced to below 100 nm, kink bands formed in Cu-Nb nanolaminates under compression testing with an initial strain rate of 10^{-3} s^{-1} [51]. The formation of kink bands was hypothesized to be related to the promotion of dislocation motion parallel to the interfaces, with these kink bands allowing for a compressive plastic strain of greater than 25 % for the Cu-Nb nanolaminates. Cui et al. confirmed the existence of kink bands in nanocomposite Cu-Mo films, where there was a relatively strong isotropy parallel to the loading direction and deformation localized in the kink bands but improved the overall plasticity [52]. Consequently, for the present Cu-Zr system, the kink-like features are likely to also contribute to the large, measured plasticity.

Fig. 6 presents representative fracture surfaces corresponding to the two hot-pressing conditions. A lower magnification view of the fracture surface in Fig. 6(a) for the 800 °C for 1 h sample shows individual particles with sizes ranging from tens to ~200 μm, confirming the sample was not fully consolidated and resulting in the lower strength. Magnified images in Fig. 6(b) and (c) revealed both brittle and ductile fracture regions, respectively. The brittle region exhibits a flat facet ~10 μm in size, as indicated by a red arrow in Fig. 6(b), with the facet surrounded by many small particles about 1 μm in diameter (yellow arrows). Intergranular fractures, associated with higher ductility, result in rough morphologies which have been reported for other nanocrystalline Cu fracture surfaces [53]. Sub-micrometer-sized dimples were observed (yellow arrows in Fig. 6(c)), approximately ten times larger than the matrix grain size. Dimples are indicative of ductile fracture and have been observed in another powder metallurgy study on nanocrystalline Cu with a similar sub-micrometer grain size [54]. In that study, a nanocrystalline Cu that was milled for 10 h exhibited mixed-mode fracture including microcracks in addition to the dimpling. Here, inclusions were occasionally observed within dimples with one example being marked by a red arrow in Fig. 6(c). As the consolidation condition increased to 900 °C for 10 h, a majority of the fracture surfaces exhibited wavy patterns, which were separated by flat surfaces shown in Fig. 6(d). Higher magnification in Fig. 6(e) of the regions with parallel lines reveal the abraded area, from where the sample failed along the dominant shear band. It is also possible that the abraded region could even have started as a ductile region but then sheared away and smeared, leaving behind thin parallel lines. Similar thin, parallel features are seen as the result of shear tests [55]. The wavy patterns were revealed to be dimple-like structures when inspected with a higher magnification in Fig. 6(f). Comparing the dimple sizes between the two conditions, the size increased from sub-micrometer to 1–2 μm as the matrix grains coarsened from 40 to 101 nm. Therefore, the dimple size seems to loosely scale with the matrix grain size and encompass multiple grains.

4. Conclusion

In conclusion, fully dense, centimeter-sized nanocrystalline Cu-rich alloys with grain sizes of ~100 nm were successfully fabricated via a simple powder metallurgy route, resulting in a good combination of strength and plasticity. The main mechanism for the improved density is

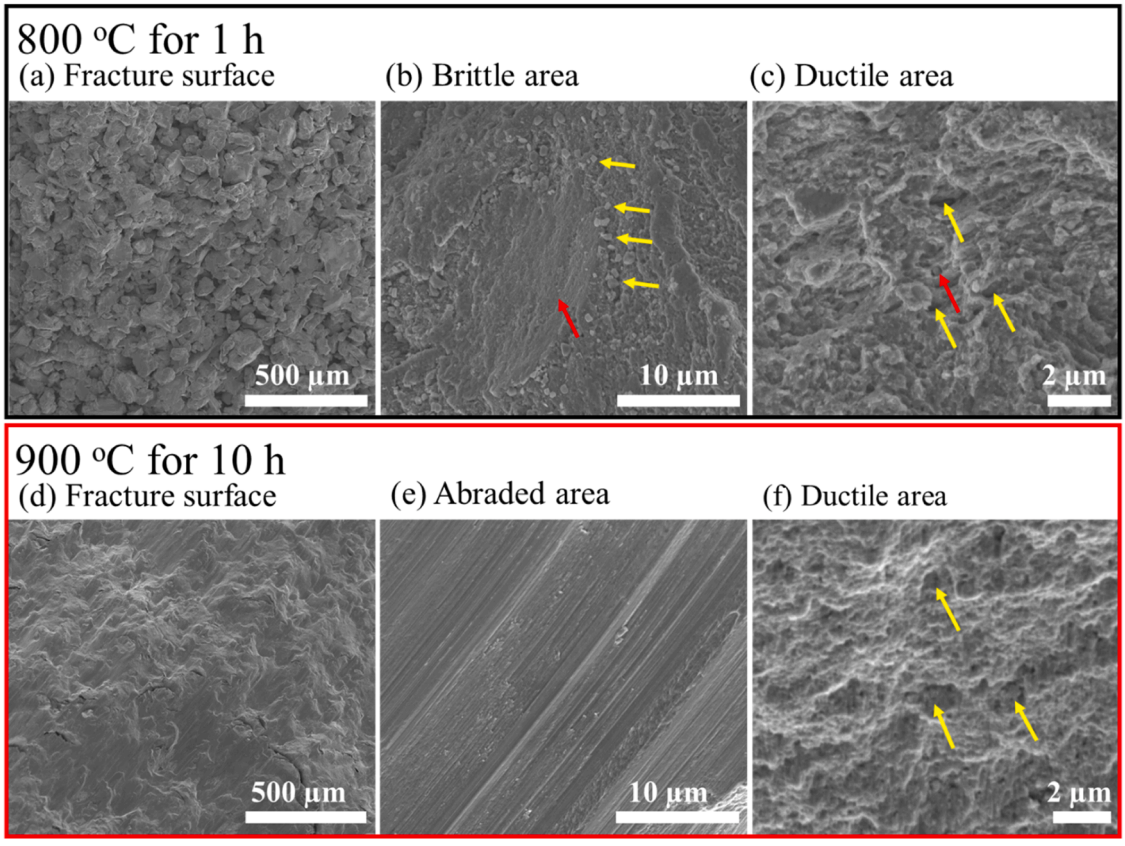

Fig. 6. SEM micrographs showing fracture surfaces of Cu-Zr samples hot pressed under (a-c) 800 °C for 1 h, resulting in a mixture of brittle and ductile fracture modes, and (d-f) 900 °C for 10 h, where the failure along the dominant shear band resulted in abraded area and ductile fracture mode.

the presence of amorphous grain boundary complexions at the high sintering temperature, as shown previously by Donaldson and Rupert [29]. These authors found that a marked increase in density was observed for the same conditions that enabled amorphous complexion formation during hot pressing. After hot pressing at 800 °C for 1 h here, the pellet had ~20 % porosity, whereas hot pressing at 900 °C for 10 h resulted in a fully dense pellet. Quasi-static bulk compression testing showed that the alloys that were consolidated to full density exhibit a combination of high strength and large compressive plasticity, with an average yield strength of 722 ± 45 MPa and an average failure strain of 25.3 ± 2.4 %. The underlying mechanisms for excellent plasticity were investigated using a variety of microscopy techniques and attributed to two primary factors. First, a much smaller crack length relative to the sample dimension dramatically delayed sample failure. Second, the activation of kink banding delayed catastrophic sample failure. Amorphous complexions, although not present in the final alloys, assist with full densification by improving the sintering of the particles and limiting matrix grain growth, ultimately resulting in improved strength. Additionally, the full densification of these bulk pieces would be important for future design of Cu-alloys and studying additional properties, e.g. where high electrical resistivity could be enabled by full densification. While this work presents a processing route free of complicated quenching treatments, it may give further benefit to stabilize amorphous complexions in the future to achieve even higher strengths and improved ductility [33,56]. Amorphous complexions have been shown to absorb dislocations better than ordered boundaries and, therefore, increase ductility. The combination of a simple processing route and common alloying element gives strengths that compete with much more expensive specialty materials in the Cu-rich class of alloys.

CRediT authorship contribution statement

Esther C. Hessong: Writing – review & editing, Writing – original draft, Investigation, Formal analysis. **Tianjiao Lei:** Writing – review & editing, Investigation. **Brandon Fields:** Writing – review & editing, Investigation. **Raphael Pierre Thiraux:** Writing – review & editing, Investigation. **Brad L. Boyce:** Writing – review & editing, Conceptualization. **Timothy J. Rupert:** Writing – review & editing, Supervision, Project administration, Methodology, Investigation, Funding acquisition, Conceptualization.

Declaration of competing interest

The authors declare that they have no known competing financial interests or personal relationships that could have appeared to influence the work reported in this paper.

Acknowledgements

This work was supported by the U.S. Department of Energy, Office of Science, Basic Energy Sciences, under Award No. DE-SC0025195. The authors acknowledge the use of facilities and instrumentation at the UC Irvine Materials Research Institute (IMRI), which is supported in part by the National Science Foundation through the UC Irvine Materials Research Science and Engineering Center (DMR-2011967). SEM, FIB, and EDS work was performed using instrumentation funded in part by the National Science Foundation Center for Chemistry at the Space-Time Limit (CHE-0802913).

References

[1] K. Fukamachi, M. Kimura, Age-hardening structure and mechanism of Cu–3at% Ni–1.5 at% Si corson alloy, Mater. Sci. Eng.: A 831 (2022) 142220.
[2] D. Li, Q. Wang, B. Jiang, X. Li, W. Zhou, C. Dong, H. Wang, Q. Chen, Minor-alloyed Cu-Ni-Si alloys with high hardness and electric conductivity designed by a cluster formula approach, Prog. Nat. Sci.: Mater. Int. 27 (4) (2017) 467–473.
[3] Z. Wang, J. Li, Z. Fan, Y. Zhang, S. Hui, L. Peng, G. Huang, H. Xie, X. Mi, Effects of Co addition on the microstructure and properties of elastic Cu-Ni-Si-based alloys for electrical connectors, Material 14 (8) (2021), 1996.
[4] M. Bauccio, ASM Metals Reference Book ASM International, 1993.
[5] L. Lu, Y. Shen, X. Chen, L. Qian, K. Lu, Ultrahigh strength and high electrical conductivity in copper, Science 304 (5669) (2004) 422–426.
[6] Y. Shen, L. Lu, Q. Lu, Z. Jin, K. Lu, Tensile properties of copper with nano-scale twins, Scr. Mater. 52 (10) (2005) 989–994.
[7] S. Semboshi, T. Takasugi, Fabrication of high-strength and high-conductivity Cu–Ti alloy wire by aging in a hydrogen atmosphere, J. Alloys. Compd. 580 (2013) S397–S400.
[8] S. Semboshi, Y. Kaneno, T. Takasugi, N. Masahashi, High strength and high electrical conductivity Cu-Ti alloy wires fabricated by aging and severe drawing, Metall. Mater. Trans. A 49 (2018) 4956–4965.
[9] L. Si, L. Zhou, X. Zhu, L. Sanhua, S. Leinuo, D. Qiyi, Microstructure and property of Cu–2.7 Ti–0.15 Mg–0.1 Ce–0.1 Zr alloy treated with a combined aging process, Mater. Sci. Eng.: A 650 (2016) 345–353.
[10] X.-Z. Zhou, Y.-C. Su, A novel Cu–Ni–Zn–Al alloy with high strength through precipitation hardening, Mater. Sci. Eng.: A 527 (20) (2010) 5153–5156.
[11] F. Dalla Torre, R. Lapovok, J. Sandlin, P.F. Thomson, C.H.J. Davies, E.V. Pereloma, Microstructures and properties of copper processed by equal channel angular extrusion for 1–16 passes, Acta Mater. 52 (16) (2004) 4819–4832.
[12] S. Li, I.J. Beyerlein, C.T. Necker, D.J. Alexander, M. Bourke, Heterogeneity of deformation texture in equal channel angular extrusion of copper, Acta Mater. 52 (16) (2004) 4859–4875.
[13] T. Hebesberger, H.-P. Stüwe, A. Vorhauer, F. Wetscher, R. Pippan, Structure of Cu deformed by high pressure torsion, Acta Mater. 53 (2) (2005) 393–402.
[14] A. Mazilkin, V. Tavakkoli, O. Davydenko, Y. Beygelzimer, E. Boltynjuk, T. Boll, B. Straumal, B. Baretzky, Y. Estrin, R. Kulagin, Mechanisms of structural evolution of laminates with immiscible components under high-pressure torsion, Acta Mater. 269 (2024) 119804.
[15] H. Wei, Y. Cui, H. Cui, C. Zhou, L. Hou, Y. hui Wei, Evolution of grain refinement mechanism in Cu-4wt.% Ti alloy during surface mechanical attrition treatment, J. Alloys. Compd. 763 (2018) 835–843.
[16] H. Yang, Y. Chen, H. Feng, P. Yang, J. Zhang, B. Shu, Optimized corrosion resistance in pure copper via surface mechanical attrition treatment and subsequent annealing, Mater. Today Commun. 35 (2023) 105645.
[17] F. Froes, D. Eylon, Powder metallurgy of titanium alloys, Int. Mater. Rev. 35 (1) (1990) 162–184.
[18] A. Munoz, B. Savoini, M. Monge, Y. Ortega, O. Dura, Fabrication and characterization of Cu reinforced with Y-enriched particles following a novel powder metallurgy route, Nucl. Mater. Energy 29 (2021) 101075.
[19] W. Zeng, J. Xie, D. Zhou, Z. Fu, D. Zhang, E.J. Lavernia, In-situ formation of NbC in nanocrystalline Cu, J. Alloys Compd. 725 (2017) 334–341.
[20] D.G. Morris, M. Morris, Microstructure and strength of nanocrystalline copper alloy prepared by mechanical alloying, Acta Metall. Mater. 39 (8) (1991) 1763–1770.
[21] Y. Wang, M. Chen, F. Zhou, E. Ma, High tensile ductility in a nanostructured metal, Nature 419 (6910) (2002) 912–915.
[22] R. Lei, S. Xu, M. Wang, H. Wang, Microstructure and properties of nanocrystalline copper–niobium alloy with high strength and high conductivity, Mater. Sci. Eng.: A 586 (2013) 367–373.
[23] K. Darling, M. Tschopp, R. Guduru, W. Yin, Q. Wei, L. Kecskes, Microstructure and mechanical properties of bulk nanostructured Cu–Ta alloys consolidated by equal channel angular extrusion, Acta Mater. 76 (2014) 168–185.
[24] E. Botcharova, J. Freudenberger, L. Schultz, Mechanical and electrical properties of mechanically alloyed nanocrystalline Cu–Nb alloys, Acta Mater. 54 (12) (2006) 3333–3341.
[25] Y. Bian, J. Ni, C. Wang, J. Zhen, H. Hao, X. Kong, H. Chen, J. Li, X. Li, Z. Jia, Microstructure and wear characteristics of in-situ micro/nanoscale niobium carbide reinforced copper composites fabricated through powder metallurgy, Mater. Charact. 172 (2021) 110847.
[26] P.C. Millett, R.P. Selvam, A. Saxena, Stabilizing nanocrystalline materials with dopants, Acta Mater. 55 (7) (2007) 2329–2336.
[27] T. Frolov, K. Darling, L. Kecskes, Y. Mishin, Stabilization and strengthening of nanocrystalline copper by alloying with tantalum, Acta Mater. 60 (5) (2012) 2158–2168.
[28] K. Sikdar, A. Mahata, B. Roy, D. Roy, Hybrid thermal stabilization of Zr doped nanocrystalline Cu, Mater. Des. 164 (2019) 107564.
[29] O.K. Donaldson, T.J. Rupert, Amorphous intergranular films enable the creation of bulk nanocrystalline Cu–Zr with full density, Adv. Eng. Mater. 21 (9) (2019) 1900333.
[30] A. Khalajhedayati, T.J. Rupert, High-temperature stability and grain boundary complexion formation in a nanocrystalline Cu-Zr alloy, JOM 67 (2015) 2788–2801.
[31] Y. Hwang, J. Kim, C. Yim, H.W. Park, Deep-sintered copper tracks for thermal oxidation resistance using large pulsed electron beam, ACS Omega 6 (29) (2021) 19134–19143.
[32] A.A. Efimov, D.V. Kornyushin, A.I. Buchnev, E.I. Kameneva, A.A. Lizunova, P. V. Arsenov, A.E. Varfolomeev, N.B. Pavzderin, A.V. Nikonov, V.V. Ivanov, Fabrication of conductive and gas-sensing microstructures using focused deposition of copper nanoparticles synthesized by spark discharge, Appl. Sci. 11 (13) (2021) 5791.
[33] A. Khalajhedayati, Z. Pan, T.J. Rupert, Manipulating the interfacial structure of nanomaterials to achieve a unique combination of strength and ductility, Nat. Commun. 7 (1) (2016) 10802.
[34] S.-W. Lee, M.-Y. Huh, E. Fleury, J.-C. Lee, Crystallization-induced plasticity of Cu–Zr containing bulk amorphous alloys, Acta Mater. 54 (2) (2006) 349–355.

[35] W.F. Smith, J. Hashemi, Materials Science and Engineering, Tata McGraw-Hill, 2008.
[36] N. Vo, J. Schäfer, R. Averback, K. Albe, Y. Ashkenazy, P. Bellon, Reaching theoretical strengths in nanocrystalline Cu by grain boundary doping, Scr. Mater. 65 (8) (2011) 660–663.
[37] L. Han, J. Wang, Y. Chen, Y. Huang, Y. Liu, Z. Wang, Fabrication and mechanical properties of WC nanoparticle dispersion-strengthened copper, Mater. Sci. Eng.: A 817 (2021) 141274.
[38] B. Hornbuckle, J. Smeltzer, S. Sharma, S. Nagar, C. Marvel, P. Cantwell, M. Harmer, K. Solanki, K. Darling, A high-temperature nanostructured Cu-Ta-Li alloy with complexion-stabilized precipitates, Science 387 (6741) (2025) 1413–1417.
[39] N.P. Suh, Fundamentals of design and deployment of large complex systems: OLEV, MH, and mixalloy, J. Integr. Des. Process Sci. 16 (3) (2012) 7–28.
[40] G.W. Lederer, N.K. Foley, B.W. Jaskula, R.A. Ayuso, Beryllium—A Critical Mineral commodity—Resources, production, and Supply Chain, US Geological Survey, 2016.
[41] T. Gordon, D. Bowser, Beryllium: genotoxicity and carcinogenicity, Mutat. Res./ Fundam. Mol. Mech. Mutagen. 533 (1–2) (2003) 99–105.
[42] S. Srinivasan, S. Sharma, S. Turnage, B. Hornbuckle, C. Kale, K. Darling, K. Solanki, Role of tantalum concentration, processing temperature, and strain-rate on the mechanical behavior of copper-tantalum alloys, Acta Mater. 208 (2021) 116706.
[43] V. Segal, Equal-channel angular extrusion (ECAE): from a laboratory curiosity to an industrial technology, Metals 10 (2) (2020) 244.
[44] Y. Macheret, A.D. Watkins, G.E. Korth, T.M. Lillo, J.E. Flinn Jr, D. Herling, M. Smith, R. Schwarz, Equal Channel Angular Extrusion Progress Report for March 1998-May 1999, Idaho National Lab.(INL), Idaho Falls, ID (United States), 1999.
[45] S. Lister, O. Levano Blanch, B. Fernández Silva, N. Weston, M. Jackson, A comparative study of microstructure and texture evolution in low cost titanium alloy swarf and powder recycled via FAST and HIP, Mater. Sci. Technol. (2024) 02670836241277060.
[46] J. Huang, Z. Xiao, J. Dai, Z. Li, H. Jiang, W. Wang, X. Zhang, Microstructure and properties of a novel Cu–Ni–Co–Si–Mg alloy with super-high strength and conductivity, Mater. Sci. Eng.: A 744 (2019) 754–763.
[47] D. Raabe, K. Miyake, H. Takahara, Processing, microstructure, and properties of ternary high-strength Cu–Cr–Ag in situ composites, Mater. Sci. Eng.: A 291 (1–2) (2000) 186–197.
[48] P.J. Noell, J.D. Carroll, B.L. Boyce, The mechanisms of ductile rupture, Acta Mater. 161 (2018) 83–98.
[49] P. Partridge, The crystallography and deformation modes of hexagonal close-packed metals, Metall. Rev. 12 (1) (1967) 169–194.
[50] M. Barsoum, L. Farber, T. El-Raghy, Dislocations, kink bands, and room-temperature plasticity of Ti 3 SiC 2, Metall. Mater. Trans. A 30 (1999) 1727–1738.
[51] T. Nizolek, N.A. Mara, I.J. Beyerlein, J.T. Avallone, T.M. Pollock, Enhanced plasticity via kinking in cubic metallic nanolaminates, Adv. Eng. Mater. 17 (6) (2015) 781–785.
[52] Y. Cui, B. Derby, N. Li, A. Misra, Design of bicontinuous metallic nanocomposites for high-strength and plasticity, Mater. Des. 166 (2019) 107602.
[53] R.K. Guduru, K.A. Darling, R.O. Scattergood, C.C. Koch, K. Murty, Mechanical properties of electrodeposited nanocrystalline copper using tensile and shear punch tests, J. Mater. Sci. 42 (2007) 5581–5588.
[54] M.A. Thein, M. Gupta, Microstructural, physical, and mechanical characteristics of bulk nanocrystalline copper synthesised using powder metallurgy, Mater. Sci. Technol. 19 (11) (2003) 1473–1477.
[55] B. Valoppi, Z. Zhang, M. Deng, A. Ghiotti, S. Bruschi, K.F. Ehmann, J. Cao, On the fracture characterization in double-sided incremental forming of Ti6Al4V sheets at elevated temperatures, Procedia Manuf. 10 (2017) 407–416.
[56] V. Turlo, T.J. Rupert, Grain boundary complexions and the strength of nanocrystalline metals: dislocation emission and propagation, Acta Mater. 151 (2018) 100–111.